Selective CO2 adsorption in water-stable alkaline-earth based metal–organic frameworks

Tang, Y.; Kourtellaris, A.; Tasiopoulos, A.J.; Teat, S.J.; Dubbeldam, D.; Rothenberg, G.; Tanase, S.

DOI
10.1039/c7qi00734e

Publication date
2018

Document Version
Final published version

Published in
Inorganic Chemistry Frontiers

Volume 5 | Number 3 | March 2018

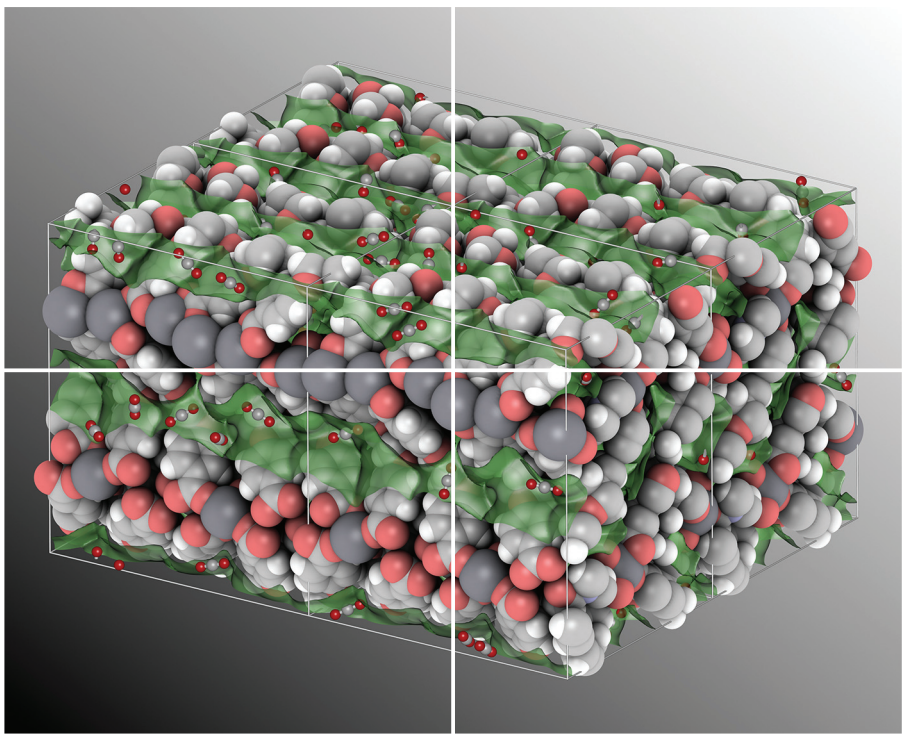

INORGANIC CHEMISTRY

FRONTIERS

Chinese Chemical Society

ROYAL SOCIETY OF CHEMISTRY

rsc.li/frontiers-inorganic

INORGANIC CHEMISTRY
FRONTIERS

RESEARCH ARTICLE

View Article Online
View Journal | View Issue

Cite this: *Inorg. Chem. Front.*, 2018, **5**, 541

Selective CO_2 adsorption in water-stable alkaline-earth based metal–organic frameworks†

Yiwen Tang,[a] Andreas Kourtellaris,[b] Anastasios J. Tasiopoulos,[b] Simon J. Teat,[c] David Dubbeldam,[a] Gadi Rothenberg[a] and Stefania Tanase*[a]

Received 21st November 2017,
Accepted 9th February 2018

DOI: 10.1039/c7qi00734e

rsc.li/frontiers-inorganic

Four novel metal–organic frameworks (MOFs) built from alkaline-earth metal ions and the flexible tetrahedral carboxylate ligand tetrakis[4-(carboxyphenyl)oxamethyl]methane acid (H_4L) were synthesized using solvothermal methods. A variety of three-dimensional frameworks were obtained when employing different alkaline earth ions with the formula $[Mg_2(L)(H_2O)(DMA)]\cdot DMA$ (**1**), $[Ca_4(L)_2(DMA)_3]$ (**2**), $[Ca_4(L)_2(H_2O)_2(DMA)_2]\cdot(3DMA)$ (**3**) and $[Sr_4(L)_2(DMF)_4]\cdot(2DMF)$ (**4**) reflecting the variation in the ionic radius of alkaline-earth ions as well as the key role of the synthetic conditions used. By removing the guest molecules, a framework shrinking was observed driven by the structural flexibility of the H_4L ligand. This resulted in large diffusional resistances towards N_2 over CO_2 molecules, therefore leading to a good CO_2/N_2 separation selectivity. Both Ca-based MOFs were very stable up to 98% relative humidity, while Mg- and Sr-based MOFs were much less stable.

Introduction

The inherent properties of metal–organic frameworks (MOFs), including high surface area, various compositions and porous networks together with their tuneable functionalities make them attractive candidates for a range of applications, including gas storage,[1] molecular separations[2] and sensing,[3] as well as catalysis.[4] A variety of metal cations and functionalized organic ligands are used to design MOFs that fulfil different functionalities. Most MOFs are predominantly built from transition metal ions and, more recently, rare-earth metal ions as nodes. Porous networks based on alkaline-earth cations are relatively rare. This is mostly due to their unpredictable coordination numbers and geometries, as well as their tendency to form solvated organic–inorganic ionic layers instead of MOFs.[5,6] Therefore, alkaline-earth ions are usually regarded as unsuitable metal nodes for forming porous structures. Recent studies, however, show the potential of alkaline-earth based MOFs with specific properties, including ionic conductivity,[7] good ferroelectricity and piezoelectricity,[8] luminescence[9] and gas separation properties.[10] Using alkaline-earth ions offers other advantages compared to the transition and lanthanide metal ions, including abundance, light weight and low costs.

Apart from metal nodes, the organic linkers also play an important role in constructing new alkaline-earth metal based MOFs. Polycarboxylate ligands, especially flexible ones, are widely used in MOF synthesis because their variable coordination modes enable a variety of framework architectures and specific chemical and physical properties.[11] Among these, tetrakis[4-(carboxypheneyl)oxamethyl]methane acid (H_4L) is a promising candidate for synthesizing MOFs.[12] Firstly, due to its four carboxylate groups, different topological networks, *dia* (diamond), *lon* (lonsdaleite), *pts* (PtS) and *flu* (CaF_2) can be obtained.[13] Secondly, removing the guest molecules from some MOFs prepared from flexible ligands, such as H_4L, can cause a framework shrinking driven by the flexible ligand distortion, leading to enhanced gas adsorption/separation properties.[14,15] Most of the MOFs built from the H_4L linker contain transition and lanthanide metal ions as metal nodes. However, to the best of our knowledge, there are no reports on alkaline-earth MOFs with this linker.

Here we report the synthesis of novel MOF structures that combine the flexible coordination behaviour of the alkaline-metal ions, with the binding versatility of the H_4L linker. Four new alkali-earth based MOFs are synthesised and characterised for their humidity stability and adsorption properties.

[a]*Van 't Hoff Institute for Molecular Sciences, University of Amsterdam, Science Park 904, 1098 XH Amsterdam, The Netherlands. E-mail: s.grecea@uva.nl*
[b]*Department of Chemistry, University of Cyprus, 1678 Nicosia, Cyprus*
[c]*Advanced Light Source, Lawrence Berkeley National Laboratory, Berkeley, California 94720, USA*

†Electronic supplementary information (ESI) available. CCDC 1582901–1582903 and 1586997. For ESI and crystallographic data in CIF or other electronic format see DOI: 10.1039/c7qi00734e

Experimental

Materials and general methods

The ligand, tetrakis[4-(carboxyphenyl)oxamethyl]methane acid (H_4L) was synthesized using a reported procedure (see Scheme S1 in ESI†).[16] All other chemicals and solvents were purchased from commercial suppliers and used as received. Infrared spectra (IR, 4000–400 cm^{-1}, resol, 0.5 cm^{-1}) were recorded on a Varian 660 FTIR spectrometer equipped with a Gladi ATR device using KBr pellets as the transmission technique. Powder X-ray diffraction (PXRD) measurements were carried out on a Rigaku Miniflex X-ray diffractometer. Measurements were done from 3° to 50° with a turning speed of 2.0° min^{-1}. Thermogravimetic analysis (TGA) and differential scanning calorimetry (DSC) measurements were carried out on a STA 449 F3 Jupiter® (NETZSCH Instrument) unit. The measurements were done under air (20 ml min^{-1}) from 35 to 800 °C. N_2 adsorption isotherms were recorded on a Thermo Scientific Surfer instrument at 77 K and 273 K, respectively. Using the same instrument, CO_2 adsorption isotherms were measured at 273 K. Water adsorption measurements at 303 K were performed in a micro-calorimeter (Calvet C80, Setaram) which can operate isothermally and is connected to a home built manometric apparatus. All the samples were completely degassed under a high vacuum ($<10^{-4}$ torr) at 423 K for 8 h before each measurement.

Synthetic procedures

$[Mg_2(L)(H_2O)(DMA)]\cdot 4DMA$ (1). In a 20 ml Telflon-capped borosilicate tube was added a solution of $Mg(NO_3)_2\cdot 6H_2O$ (25.6 mg, 0.1 mmol) and H_4L (61.6 mg, 0.1 mmol) in a solvent mixture of *N*,*N*-dimethylacetamide (DMA, 9 ml)/water (1 ml). The vial was then sealed and placed in an oven at 150 °C for 48 h. Colourless crystals were then collected by filtration and washed with fresh DMA several times, and dried at room temperature. Yield: 80%. IR (KBr, cm^{-1}): 2944 (w), 1620 (s), 1547 (m), 1452 (w), 1398 (s), 1230 (s), 1171 (m), 1017 (s), 858 (m), 785 (s), 681 (m). C, H, N analysis (%): calcd C 57.17, H 6.20, N 6.29; found C 57.58, H 6.37, N 6.18.

$[Ca_4(L)_2(DMA)_3]\cdot 7H_2O$ (2). In a 20 ml Telflon-capped borosilicate tube was added a solution of $Ca(OH)_2$ (7.4 mg, 0.1 mmol) and H_4L (61.6 mg, 0.1 mmol) in a solvent mixture of DMA (9 ml)/water (1 ml). The vial was then sealed and placed in an oven at 120 °C for 48 h. Colourless cubic crystals were then obtained and separated by filtration and washed with fresh DMA several times, then dried at room temperature. Yield: 72%. IR (KBr, cm^{-1}): 2944 (w), 1683 (s), 1606 (s), 1561 (s), 1430 (m), 1238 (s), 1035 (m), 862 (s), 780 (s), 654 (m). C, H, N analysis (%): calcd C 52.82, H 5.02, N 2.37; found C 52.49, H 4.80, N 2.47.

$[Ca_4(L)_2(H_2O)_2(DMA)_2]\cdot 3DMA$ (3). The synthetic procedures of **3** is the same as for compound **2**, but with the reaction temperature set at 140 °C. Yield: 72%. IR (KBr, cm^{-1}): 2940 (w), 1622 (s), 1529 (m), 1420 (s), 1302 (w), 1234 (s), 1171 (m), 1017 (m), 862 (m), 789 (s), 654 (m). C, H, N analysis (%): calcd C 55.57, H 5.22, N 3.76; found C 55.33, H 5.03, N 3.36.

$[Sr_4(L)_2(DMF)_4]\cdot 2DMF$ (4). In a 20 ml Telflon-capped borosilicate tube was added a solution of $Sr(NO_3)_2$ (21.2 mg, 0.1 mmol) and H_4L (61.6 mg, 0.1 mmol) in a solvent of *N*,*N*-dimethylformamide (DMF, 10 ml). The vial was then sealed and placed in an oven at 150 °C for 48 h. Colourless crystals were then formed by filtration, washed with fresh DMF several times and dried at room temperature. Yield: 65%. IR (KBr, cm^{-1}): 2940 (w), 1656 (s), 1611 (s), 1547 (m), 1420 (w), 1380 (s), 1238 (s), 1162 (m), 1026 (m), 862 (m), 780 (s), 672 (m). C, H, N analysis (%): calcd C 50.05, H 4.47, N 4.17; found C 49.40, H 4.63, N 4.45.

Structure determination and refinement

Single crystal X-ray diffraction data for compounds **1**, **2** and **4** were collected on an Oxford-Diffraction Supernova diffractometer, equipped with a CCD area detector utilizing Cu Kα (λ = 1.5418 Å) radiation. A suitable crystal was mounted on a Hampton cryoloop with Paratone-N oil and transferred to a goniostat where it was cooled for data collection. Empirical absorption corrections (multiscan based on symmetry-related measurements) were applied using CrysAlis RED software.[17] The structures were solved by direct methods using SIR2004 and refined on F^2 using full-matrix least-squares with SHELXL-2014/7.[18,19] Software packages used were as follows: CrysAlis CCD for data collection, CrysAlis RED for cell refinement and data reduction, WINGX for geometric calculations, and DIAMOND and Mercury for molecular graphics.[20] The non-H atoms were treated anisotropically, whereas the aromatic H atoms were placed in calculated, ideal positions and refined as riding on their respective carbon atoms. Electron density contributions from disordered guest molecules were handled using the SQUEEZE procedure from the PLATON software suit.[21]

Single crystal X-ray diffraction data for compound **3** were collected on the Advanced Light Source on beamline 11.3.1 using a Bruker diffractometer, equipped with a PHOTON2 CPAD area detector utilizing synchrotron (λ = 0.7749 Å) radiation. A suitable crystal was mounted on a MiTeGen microloop with Paratone-N oil and transferred to a goniostat where it was cooled to 220 K for data collection. Empirical absorption corrections (multiscan based on symmetry-related measurements) were applied using SADABS software.[22] The structure was solved by direct methods using SHELXT and refined on F^2 using full-matrix least-squares with SHELXL-2014/7.[18,19] Software packages used were as follows: APEX3 for data collection, cell refinement and data reduction, WINGX for geometric calculations, and DIAMOND and Mercury for molecular graphics.[20] The non-hydrogen atoms were treated anisotropically, whereas the aromatic hydrogen atoms were placed in calculated, ideal positions and methyl hydrogen atoms were found in the difference map, all were refined as riding on their respective carbon atoms.

The detailed crystallographic data are shown in ESI (see ESI, Table S1†). CCDC 1582901–1582903 and 1586997† contain the supplementary crystallographic data for this paper.

Results and discussion

Description of the crystal structures

Four alkaline-earth based MOFs were synthesized using various alkaline-earth salts and tetrakis[4-(carboxypheneyl)oxamethyl]methane acid (H_4L) as starting materials. This was done by varying both the type of alkaline-earth salt as well as the temperature of the hydrothermal reaction. In all cases, highly crystalline materials were obtained and their purity was confirmed by using a combination of techniques, including single-crystal and powder XRD, FTIR spectroscopy, thermogravimetric analysis (TGA) and gas adsorption measurements.

Representations of the secondary building unit (SBU) and the porous framework of **1** are shown in Fig. 1. Compound **1** crystallizes in the orthorhombic space group P_{bca}. The asymmetric unit consists of two crystallographically independent Mg^{2+} centers (Mg1 and Mg2), one fully deprotonated L^{4-} organic linker, two DMA and one water molecules. Although both Mg^{2+} centers are surrounded by six oxygen atoms displaying distorted octahedral coordination geometry, their coordination spheres are not equivalent as shown in Fig. 1a. Particularly, Mg1 is linked to two oxygen atoms from one chelating carboxylate ligand and three oxygen atoms of bridging carboxylate groups from four different L^{4-} linkers as well as one oxygen atom from a coordinated DMA molecule. The Mg1–O bond lengths range from 2.031 to 2.162 Å. Mg2 is linked to six oxygen atoms provided from five carboxylate groups of four independent L^{4-} linkers and one terminal water molecule. The Mg2–O bond lengths range from 2.119 to 2.215 Å. The carboxylate bridges of each L^{4-} adopt a distorted tetrahedral conformation with the angle between the four arms ranging from 108° to 112°. Three of the carboxylate groups of the tetracarboxylic ligand L^{4+} bridge two Mg^{2+} ions either in the common bridging μ_2–η^1,η^1 mode (two of them) or in a bridging-chelating μ_2–η^2,η^1 mode and the fourth one bridges three Mg^{2+} ions in a μ_3–η^1,η^2 mode (see Fig. 1c).

The two types of MgO_6 octahedra are connected by one *syn–syn* carboxylate group and two monoatomic oxygen bridges resulting in a dinuclear Mg_2 unit. The dinuclear units are linked through triatomic bridges of μ_2–η^1,η^1 and μ_3–η^1,η^2 carboxylates, resulting in the formation of the tetranuclear $[Mg_4(CO_2)_8(H_2O)_2(DMA)_2]$ SBU of **1** (see Fig. 1a and b). Then as shown in Fig. 1d, each L^{4-} ligand connects three SBUs creating a three-dimensional (3D) coordinated framework. The key feature of the 3D framework of **1** is the presence of one-dimensional (1D) rhombic channels that run along the *a* direction. These channels are occupied by the guest and coordinated solvent molecules. The solvent accessible volume calculated by PLATON is 2254.1 $Å^3$, corresponding 29.2% of the unit cell volume of **1**.

Representations of a part of the chain SBU and the 3D structure of **2** are shown in Fig. 2. Compound **2** crystallizes in the orthorhombic space group P_{bca}. The asymmetric unit contains four crystallographically independent Ca^{2+} centers, two fully deprotonated L^{4-} ligands and three coordinated DMA solvent molecules. As shown in Fig. 2a, three of the Ca^{2+} ions,

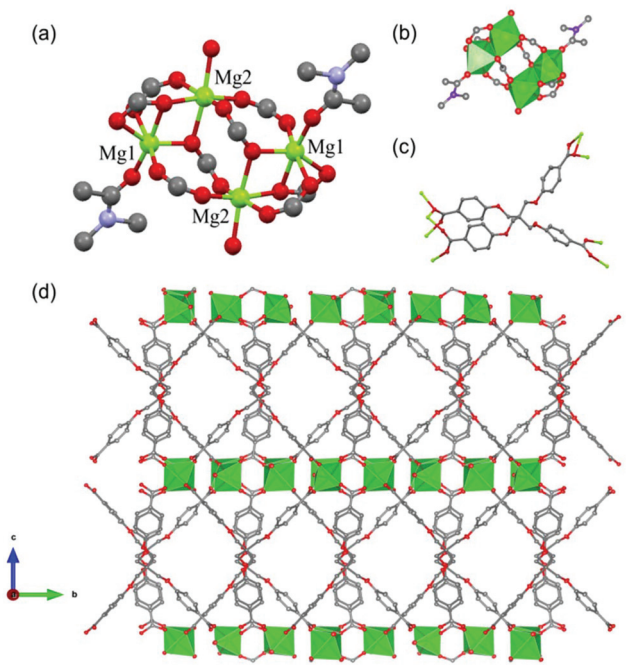

Fig. 1 (a) The local coordination environment of the Mg_4 SBU in **1**. (b) Representation of the Mg_4 SBU from edge-sharing Mg_2 octahedra units. (c) The coordination of L^{4-} ligand to the Mg^{2+} ions. (d) The porous framework with 1D rhombic channels along the *a* direction. Hydrogen atoms and solvent molecules are omitted for clarity. Mg, green; C, grey; O, red; N, purple.

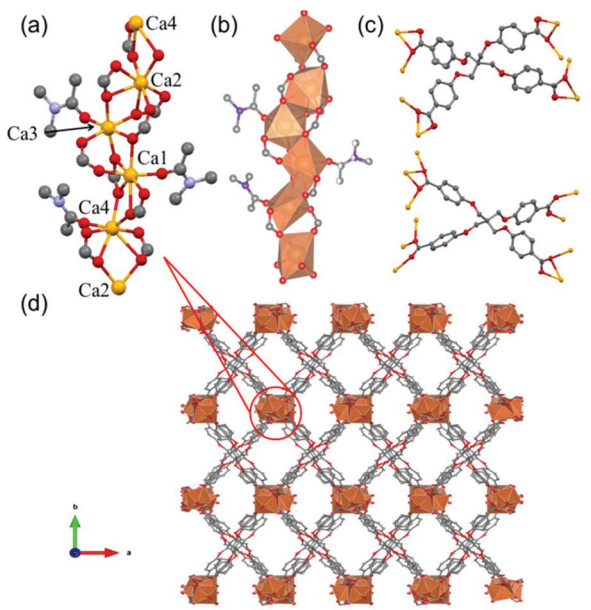

Fig. 2 (a) The local coordination environment of the 1D $[Ca_4(CO_2)_8(DMA)_3]_\infty$ rod in **2**. (b) Representation of this rod from edge-sharing Ca polyhedrons. (c) The coordination modes of the L^{4-} ligand. (d) The 3D porous framework with 1D rhombic channels along the *c* axis. Hydrogen atoms and solvent molecules are omitted for clarity. Ca, Orange; C, grey; O, red; N, purple.

Ca1, Ca2 and Ca4 centers are heptacoordinated exhibiting a distorted pentagonal bipyramidal coordination geometry whereas the fourth one, Ca3 is hexacoordinated displaying a distorted octahedral geometry. The coordination sphere of Ca1 and Ca4 consists of six oxygen atoms coming from two chelating and two bridging carboxylate groups of four L^{4-} linkers and the seventh one from a coordinated DMA molecule. Similarly, the coordination environment of Ca2 consists of five oxygen atoms, originating from two chelating and one bridging carboxylate groups located as the equatorial plane and two more from bridging carboxylate oxygen atoms occupying the axial positions of the pentagonal bipyramid. The Ca–O bond lengths range from 2.264 to 2.847 Å. The fourth Ca^{2+} ion of compound **2**, Ca3 is bound to five oxygen atoms from five bridging carboxylate groups of four L^{4-} linkers and to one oxygen atom from a coordinated DMA molecule. The Ca–O bond lengths range from 2.289 to 2.382 Å.

Fig. 2c shows that the carboxylate groups of the fully deprotonated L^{4-} organic linker in **2** display four different coordination modes. In particular, six of the carboxylate groups bridge two Ca^{2+} ions either in a bridging-chelating μ_2–η^2,η^1 mode (five carboxylates) or in the common bridging μ_2–η^1,η^1 mode (one carboxylate) and the other two carboxylate groups bridge three Ca^{2+} ions either in a μ_3–η^1,η^2 or in a μ_3–η^1,η^2,η^1 modes. The connection of the Ca^{2+} ions through carboxylate ligands gives a tetranuclear $[Ca_4(CO_2)_8(DMA)_3]$ repeating unit. The $[Ca_4(CO_2)_8(DMA)_3]$ units are connected through bridging carboxylates leading to a zig-zag chain which forms the SBU of **2** (see Fig. 2a and b). The chains are bridged through the L^{4-} linkers in the *ab* plane, forming a 3D framework with 1D rhombic channels running along the *c* axis. These channels are filled with coordinated DMA molecules. The solvent accessible volume (calculated by PLATON) is 7277 $Å^3$, corresponding to 40% of the unit cell volume of **2**. This large void volume combined with the linker flexibility favours the replacement of DMA guest molecules by water molecules upon exposure of **2** at ambient conditions.

Interestingly, even though compounds **2** and **3** are synthesized under the same experimental conditions (except the temperature of the solvothermal reaction which is 120 °C for **2** and 140 °C for **3**), their crystal structure is completely different. Fig. 3 shows the representations of a part of the chain SBU and the 3D structure of **3**. In this case, compound **3** crystallizes in the orthorhombic space group $C222_1$. The asymmetric unit comprises three crystallographically independent Ca^{2+} centers, two fully deprotonated L^{4-} linkers and five DMA molecules. Fig. 3a shows that two of the Ca^{2+} ions, Ca1 and Ca2, are hexacoordinated, displaying a distorted octahedral geometry. Conversely, Ca3 is heptacoordinated, with a distorted pentagonal bipyramidal coordination geometry. In this case, Ca1 is linked to six oxygen atoms provided from six bridging carboxylate groups of six independent L^{4-} ligand. The coordination environment of Ca2 consists of four oxygen atoms coming from four bridging carboxylate groups of four different L^{4-} linkers and two more oxygen atoms originating from two coordinated DMA molecules. The Ca–O bond lengths

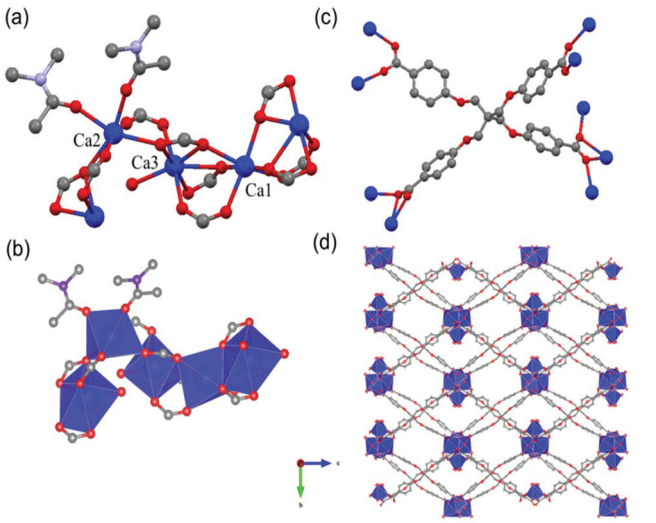

Fig. 3 (a) The local coordination environment of the $[Ca_3(CO_2)_5(H_2O)(DMA)_2]$ cluster in **3**. (b) Representation of the Ca3 cluster from vertex-sharing Ca polyhedrons. (c) The coordination of L4- ligand to the Ca^{2+} ions. (d) The porous framework with 1D rhombic channels along the a direction. Hydrogen atoms and solvent molecules are omitted for clarity. Ca, blue; C, grey; O, red; N, purple.

range from 2.218 to 2.394 Å. Ca3 binds to seven oxygen atoms from two chelating and two bridging carboxyl groups of four L^{4-} linkers and one oxygen atom from coordinated water. The Ca–O bond lengths range from 2.306 to 2.572 Å.

Fig. 3c shows that three carboxylate groups of the L^{4-} ligand bridge two Ca^{2+} ions either in the common bridging μ_2–η^1,η^1 mode (two of them) or in a bridging-chelating μ_2–η^2,η^1 mode. The fourth carboxylate group bridges three Ca^{2+} ions in a μ_3–η^1,η^2,η^1 mode. This leads to a completely different trinuclear $[Ca_3(CO_2)_5(H_2O)(DMA)_2]$ repeating unit compared with compound **2**. Similar to compound **2**, these units are connected through bridging carboxylate groups expanding to an infinite chain along a direction and the L^{4-} linkers bridge these chains into a 3D framework (see Fig. 3d). One-dimensional rhombic channels run along the *a* direction and are occupied by the guest and coordinated DMA solvent molecules. The solvent accessible volume calculated by PLATON is 2094 $Å^3$, corresponding to 23% of the unit cell volume of **3**.

Fig. 4 shows representations of a part of the chain SBU and the 3D structure of compound **4**. This compound crystallizes in the triclinic space group $P\bar{1}$. The asymmetric unit comprises four crystallographically independent Sr^{2+} centers, two L^{4-} linkers and six DMF molecules. All the Sr^{2+} ions are bound to eight oxygen atoms. In particular, Sr1 is bound to five oxygen atoms coming from one chelating and three bridging carboxylate groups of three L^{4-} ions and three oxygen atoms originating from three coordinated DMF molecules, one of which acts as terminal and the other two as bridging ligands. Sr2 is coordinated to six oxygen atoms of two chelating and two bridging carboxylate groups of three L^{4-} linkers and to two oxygen atoms of bridging DMF molecules. Sr3 binds to seven oxygen

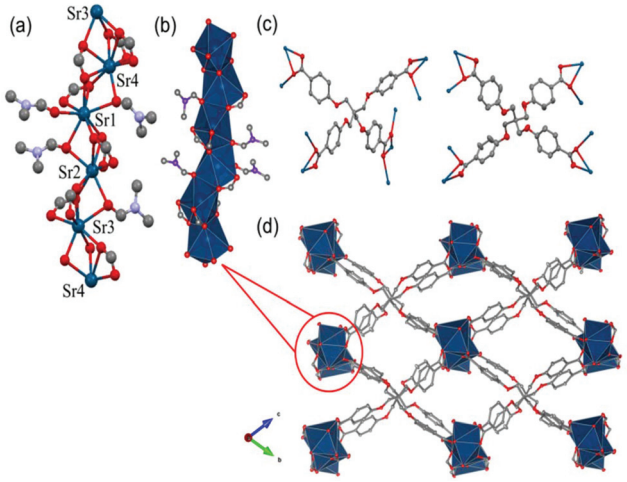

Fig. 4 (a) The local coordination environment of the $[Sr_4(CO_2)_8(DMF)_4]_\infty$ rod in **4**. (b) Representation from edge-sharing Sr polyhedrons. (c) The coordination modes of the L^{4-} ligand. (c) The 3D porous framework with 1D rhombic channels along the *a* direction. Hydrogen atoms and solvent molecules are omitted for clarity. Sr, dark blue; C, grey; O, red; N, purple.

atoms from two chelating and three bridging carboxylate groups of five L^{4-} linkers, and one oxygen atom from a bridging DMF molecule. Sr4 binds to seven oxygen atoms from three chelating and one bridging carboxylate groups of four L^{4-} linkers, and to one oxygen atom of a bridging DMF molecule. The Sr–O bond lengths vary from 2.463 to 2.737 Å.

The carboxylate groups of the fully deprotonated L^{4-} organic linker in **4** display two different coordination modes (see Fig. 4c). Specifically, seven of the carboxylate groups bridge two Sr^{2+} ions in a bridging-chelating μ_2-η^2,η^1 mode, while the eighth bridges three Sr^{2+} ions in a μ_3-η^1,η^2,η^1 mode. In addition, three of the coordinated DMF molecules act as bridging ligands connecting two Sr^{2+} ions through their O atom and the fourth one acts as a terminal ligand. The connection of the Sr^{2+} ions through carboxylate and bridging DMF ligands results in a tetranuclear $[Sr_4(CO_2)_8(DMF)_4]$ repeating unit which is linked to the neighbouring units to give an infinite chain which is the SBU of compound **4** (see Fig. 4a and b). Similar to compound **2**, the chains are linked by the L^{4-} ligands resulting a 3D framework with 1D rhombic channels running along the *a* direction. These channels are filled with coordinated and guest DMF molecules (see Fig. 4d). The solvent accessible volume calculated by PLATON is 1673 $Å^3$, corresponding to 36% of the unit cell volume of **4**.

Compounds **1–4** exhibit four distinct crystal structures, including a variety of SBUs and coordination modes of the L^{4-} ligand. This shows a clear trend in the connectivity of various alkaline-earth metal ions with the same ligand H_4L. The ionic radius increases from Mg^{2+} to Sr^{2+}, leading to an increase of the coordination number from 6 for Mg^{2+} to 8 in the case of Sr^{2+}. This is likely due to the decreased charge density of the metal ions with larger ionic radius, and their tendency to complete the coordination sphere by π-interactions with the aromatic ligand L^{4-}.[23] Moreover, the coordination flexibility of the larger ions, *e.g.* Ca^{2+}, is also reflected in the different crystal structures when the reaction conditions are changed.

Like compound **1**, several divalalent transition metal based MOFs contain metal ions, *e.g.* Zn^{2+},[24] Co^{2+} and Mn^{2+},[13] with low coordination numbers ranging from 4 to 6. All these compounds form 3D frameworks which are constructed from multiple-nuclear metal clusters as SBUs. Conversely, lanthanide ions, *e.g.* Dy^{3+},[25] La^{3+} and Eu^{3+},[14] have higher coordination numbers and form 1D metal ion-carboxyl chains of metal ions as SBUs. In compound **2**, **3** and **4**, the alkaline-earth ions have large coordination numbers, *e.g.* 7 and 8, similar to lanthanide-metal ions, and therefore they also form infinite 1D SBUs. This trend suggests that the diversity of coordination modes of the alkaline-earth metal ions can lead to extended networks similar to those obtained with transition- and lanthanide metal ions. Therefore, similar properties derived from similar structures can provide us a new choice to solve practical issues by using low-cost and non-toxic alkaline-earth metal ions instead of transition/lanthanide metal ions.

Thermal stability and gas adsorption studies

The phase purity of all four materials was confirmed by both PXRD and single-crystal X-ray diffraction analysis as well as elemental and thermogravimetric (TGA analysis). For the as-synthesised compounds **1**, **2** and **3**, the main peaks of the experimental PXRD patterns are in good agreement with the simulated ones (for details, see Fig. S1 to S3 in the ESI†). The small shift observed in the position of the peaks is due to the crystal weathering effect caused by the structural flexibility of the organic linker. This is in agreement with our observations during the single-crystal XRD measurements, the elemental analysis and the TGA analysis discussed below. The larger differences observed for **4** are assigned to a more significant arrangement which is very likely the result of the flexible coordination geometry of the Sr^{2+} ion.

Fig. 5b shows that all four compounds are stable up to *ca.* 400 °C in air. They start decomposing above this temperature. Compound **1** shows a one-step weight loss of about 26% (calc. 27%) in the 105–175 °C range, indicating the removal of all guest DMA and coordinated water molecules as well as half coordinated DMA molecule. In the temperature range 35–125 °C, the TGA of **2** displays a weight loss of about 5% (calc. 6%) corresponding to the removal of seven water molecules, thus supporting the crystal weathering effect. Furthermore, the weight loss of about 16% (calc. 15%) observed in the range 125–265 °C corresponds to the three DMA coordinated molecules. Compound **3** exhibits a continuous weight loss of about 12% (calc. 14%) in the 100–250 °C range, corresponding to the removal of guest DMA molecules. For **4**, the TGA shows a continuous weight loss of about 20% (calc. 21%) in the 130–350 °C temperature range, in agreement with the removal of all the guest and some coordinated DMF molecules.

The high thermal stability of these four frameworks encouraged us to examine their porosity and gas adsorption properties, since the removal of the guest and coordinated solvent

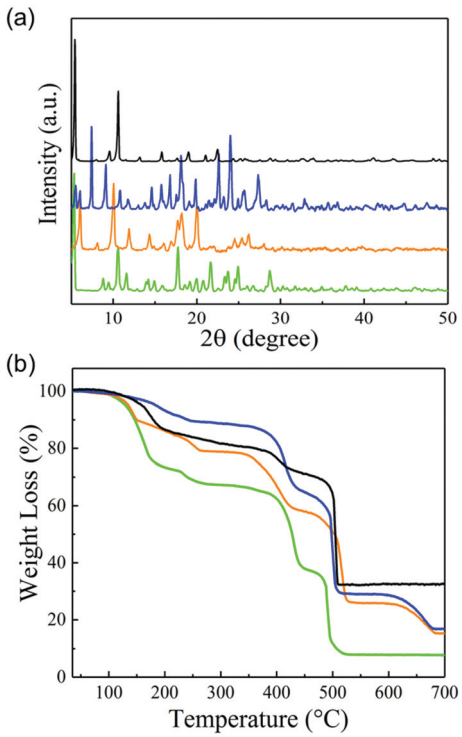

Fig. 5 (a) PXRD patterns and (b) TGA curves of the as-synthesized alkaline-earth based MOFs. Colour code: **1** (green), **2** (orange), **3** (blue) and **4** (black).

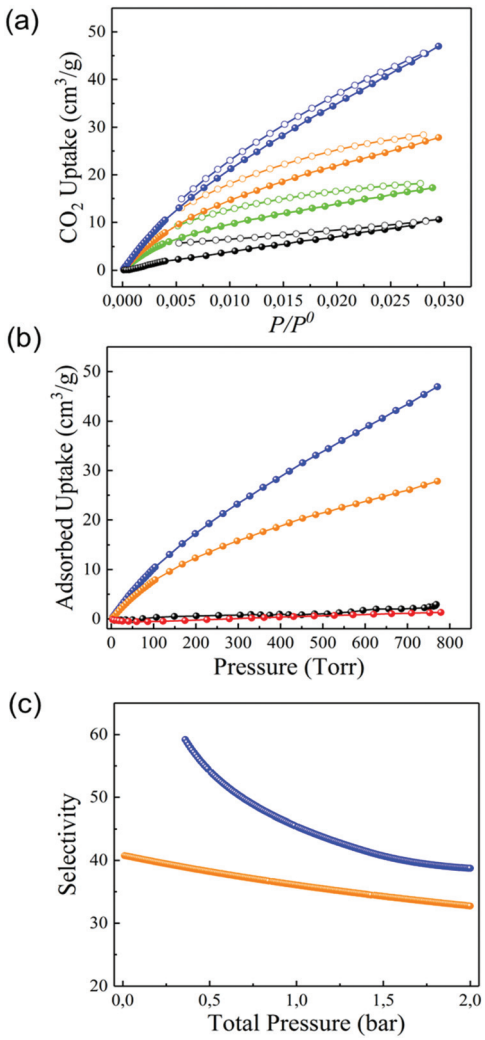

Fig. 6 (a) CO_2 uptake of the alkaline-earth based MOFs **1–4**. (Closed symbols correspond to the adsorption and the open symbols to the desorption); (b) the selective uptake of CO_2 over N_2 for **2** and **3** at 273 K; colour code: **2** (CO_2: orange, N_2: red), **3** (CO_2: blue, N_2: black). (c) IAST calculated selectivity based on the experimentally observed adsorption isotherms of the pure gases. Colour code: **2** (orange) and **3** (blue).

molecules would leave a considerable volume for adsorbing other gas molecules. To effectively remove the solvent molecules and ensure that the crystal structure is retained, we designed a suitable activation process. Thus, all compounds were heated at 150 °C under high vacuum ($<10^{-4}$ torr) for 8 h before adsorption measurements. The TGA and elemental analysis (see Fig. S5–S8 and Table S2 in the ESI†) on the activated samples **1–4** indicate that all the guest molecules are removed. Additionally, **1** lost its coordinated water and half coordinated DMA molecules, **2** lost two thirds of coordinated DMA molecules and **4** lost three fourths of coordinated DMF molecules, respectively.

To check if the evacuated materials have any porosity, we carried out N_2 adsorption measurements on all activated samples (see Fig. S9†). Surprisingly, there was almost no N_2 uptake for all materials (less than 10 $cm^3\ g^{-1}$ at STP), even though the single-crystal XRD analysis reveals that the alkaline-earth MOFs have seemingly considerable pore volume and suitable pore size for N_2 uptake. This would indicate that these compounds are either nonporous or have micro-pores smaller than the kinetic diameter of N_2 molecules (3.64 Å). To confirm this, we performed CO_2 adsorption measurements which indeed demonstrate that all four desolvated materials adsorbed CO_2 (see Fig. 6a), with a maximum uptake of 17.3 $cm^3\ g^{-1}$ (**1**), 27.6 $cm^3\ g^{-1}$ (**2**), 46.9 $cm^3\ g^{-1}$ (**3**), and 9.8 $cm^3\ g^{-1}$ (**4**), respectively.

Based on the combined N_2 and CO_2 single adsorption isotherms, we can conclude that compounds **1–4** have micropores with the size between 3.3 Å (CO_2) and 3.64 Å (N_2). Derived from the CO_2 adsorption isotherms, the specific Dubinin surface areas and micropore volumes are 182 $m^2\ g^{-1}$/0.039 $cm^{-3}\ g^{-1}$ for **1**, 355 $m^2\ g^{-1}$/0.080 $cm^{-3}\ g^{-1}$ for **2**, 576 $m^2\ g^{-1}$/0.13 $cm^{-3}\ g^{-1}$ for **3** and 71 $m^2\ g^{-1}$/0.018 $cm^{-3}\ g^{-1}$ for **4**, respectively. These values are smaller than those determined based on the single crystal XRD analysis.

To fully understand the lower surface area and pore volume values, we measured the PXRD patterns of compounds **1–4** after activation (see Fig. S1–S4 in the ESI†). The results indicate that the crystallinity of all samples decreased as compared to that of the as-synthesized frameworks. Additionally, the PXRD patterns of compounds **1** and **4** show a shift of the diffraction lines. Two factors can explain this behaviour. Firstly, a channel shrinking, collapse or blockage can occur

upon the removal of guest molecules. This is a common phenomenon observed in MOFs built from flexible linkers.[26] Secondly, some of the coordination bonds within MOF structure can break during the activation process leading to a decrease in the crystallinity.[27] The two calcium MOFs retain their crystallinity better, in agreement with the observed higher CO_2 uptake (see Fig. S1–S4 in the ESI†).

Based on the discussion above, we conclude that while compounds **1–4** are thermally stable, all of them undergo channel shrinking due to the intrinsic flexible property of ligand L^{4-} after activation. This narrows the pore diameter to a value between kinetic diameters of CO_2 (3.3 Å) and N_2 (3.64 Å). The higher stability and adsorption selectivity towards CO_2 of compounds **2** and **3** inspired us to test their potential application for separating CO_2 from N_2. This application is important, since it would be a key step in the process for removing CO_2 from the atmosphere.[28–30] As shown in Fig. 6b, there is still no N_2 adsorption for the two Ca-MOFs at 273 K. This may be due to the pore size of fully desolvated which probably is in the middle of 3.3 Å (CO_2) to 3.64 Å (N_2). The removal of the solvent molecules may cause a pore shrinking driven by the flexible ligand distortion, giving rise to large diffusional resistances towards N_2 molecules.[31] The selective adsorption of CO_2 over N_2 within compounds **2** and **3** can also be due to the strong dipole–quadrupole interaction between the highly polarizing unsaturated calcium sites after activation and the CO_2 quadrupolar molecules.[32] The binary CO_2/N_2 selectivities at 273 K with 15 : 85 molar ratios (a typical composition for power plant flue gases), are predicted by employing the ideal adsorbed solution theory (IAST) method based upon the experimental single-component CO_2 and N_2 adsorption isotherms at the same temperature (see Fig. 5c for details). Using the BET and Henry's law equation to fit the data, we find that the calculated CO_2/N_2 selectivities are in the range of 41–32 and 60–38 for compounds **2** and **3**, respectively (see Fig. S10–S13 in the ESI†). Combining the fitting data in Fig. S13,† we obtain a very low N_2 adsorbed amount until 0.35 bar at 273 K for **3**. This leads to a very high selectivity for **3** at low pressures. Therefore, only the selectivities in the range of 0.35–2 bar of compound **3** are presented in Fig. 6c. The predicted CO_2/N_2 selectivities of compound **2** and **3** at 1 bar, which is the total pressure of flue gas from a typical power plant, are 36 and 45, respectively. These values are higher than those reported for other MOFs including CAU-1 (34),[33] $[Cu_3(BTB)^{6-}]_n$ (34.2),[34] HKUST-1 (13),[35] MIL-101(Cr) (11),[36] ZIF-90 (3.5) and ZIF-69 (21).[37]

To further probe the porosity of **2** and **3**, we decided to study their stability and adsorption properties in the presence of water. The water molecule is polar and has a kinetic diameter (2.65 Å), smaller than that of the CO_2 molecule. Usually, water causes severe damage to MOF materials because moisture conditions can hardly be avoided in practical applications. The liquid-phase water adsorption studies at 303 K show that **2** and **3** exhibit water uptake capacities up to 0.84 mmol g^{-1} (**2**) and 0.93 mmol g^{-1} (**3**) at saturation pressure. These results confirm our hypothesis that the compounds have micropores which are only accessible to molecules with a small kinetic diameter. The measured enthalpies of water adsorption at low water loading are −67.9 and −66.4 kJ mol^{-1} for **2** and **3**, respectively (see Fig. 7b). This large exothermic heat effect suggest that water is strongly bound to the open sites of the Ca^{2+} ions, which are formed by removing the coordinated DMA molecules. Moreover, the rich oxygen environment within frameworks **2** and **3** plays a key role in the water uptake, favouring the formation of hydrogen bonding interactions.[38,39] Notably, the PXRD analysis indicate that **2** and **3** retain their crystal structures after water adsorption measurements. To further check the water stability, we exposed both calcium frameworks to 98% relative humidity for two weeks. Fig. S2 and S3† show that both compounds retain their crystal structure although there is some loss of crystallinity. Control experiments showed that compounds, **1** and **4** lost their crystallinity

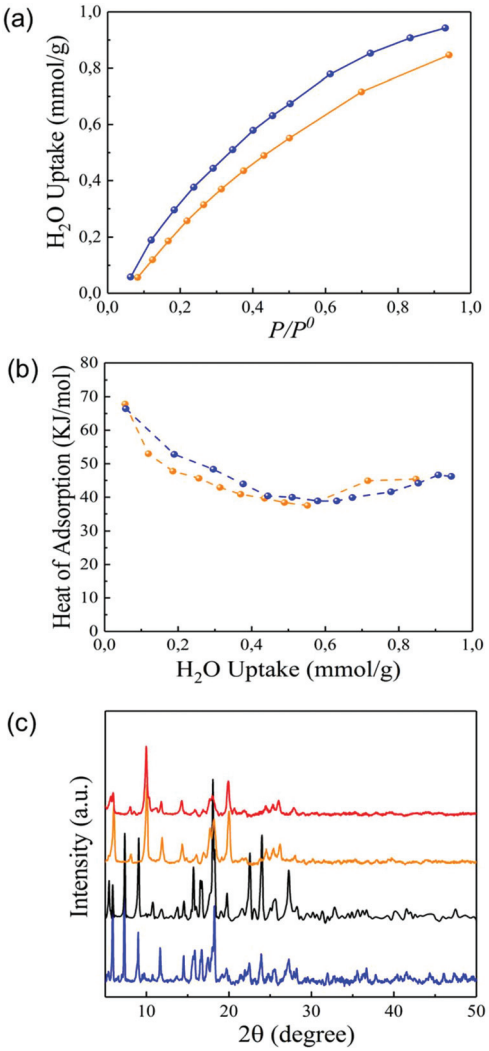

Fig. 7 (a) Water uptake of calcium-based MOFs **2** and **3** at 303 K; (b) isosteric enthalpy of water adsorption of **2** and **3** at 303 K; colour code: **2** (orange) and **3** (blue). (c) PXRD patterns of **2** and **3** before and after water adsorption. Colour code: **2** (as-synthesized: orange, after water adsorption: red) and **3** (as-synthesized: blue, after water adsorption: black).

at large extent even after 24 h under identical experimental conditions.

The results discussed above clearly indicate that the flexible L^{4-} ligand can drive a shrinking of the frameworks **1–4** after their activation, thus providing suitable pores to selective adsorb CO_2 from CO_2/N_2 mixture. Owing to the distortion of L^{4-} ligand, a specific steric arrangement of L^{4-} within framework **2** and **3** after activation causes the hydrophobic benzene rings of L^{4-} ligand to protect Ca^{2+} ions from attacking by water molecules, leading to a good humidity stability.

Conclusions

Versatile coordination behaviour and flexible structural topologies were identified in four new MOFs constructed from the H_4L polycarboxylate linker and Mg^{2+}, Ca^{2+} and Sr^{2+} metal ions. Upon removing the guest solvent molecules, the Ca-based MOFs display a flexible structural distortion which results in permanent microporosity as well as selective CO_2 uptake. The Ca MOFs can separate CO_2 over N_2 selectively, as shown by the gas adsorption experimental studies and ideal adsorbed solution theory (IAST) calculations. The same materials also have a good stability in the presence of water, demonstrated by the structural studies performed on the samples' water adsorption measurements and those exposed at 98% relative humidity. All these findings suggest that these new metal–organic frameworks built from alkaline-earth metals and flexible ligands may provide insight in developing new low-cost and non-toxic materials for gas separation applications.

Conflicts of interest

There are no conflicts to declare.

Acknowledgements

Y. T. acknowledges the China Scholarship Council (CSC) for a PhD fellowship. We thank Dr M. C. Mittelmeijer-Hazeleger (UvA) for adsorption measurements. This research used resources of the Advanced Light Source, which is a DOE Office of Science User Facility under contract no. DE-AC02-05CH11231. This work is part of the Research Priority Area Sustainable Chemistry of the University of Amsterdam, http://suschem.uva.nl.

Notes and references

1 Y. He, W. Zhou, G. Qian and B. Chen, *Chem. Soc. Rev.*, 2014, **43**, 5657.
2 Y. Basdogan, K. B. Sezginel and S. Keskin, *Ind. Eng. Chem. Res.*, 2015, **54**, 8479–8491.
3 X. Lv, K. Wang, B. Wang, J. Su, X. Zou, Y. Xie, J. Li and H. Zhou, *J. Am. Chem. Soc.*, 2017, **139**, 211–217.
4 X. Kong, Z. Lin, Z. Zhang, T. Zhang and W. Lin, *Angew. Chem., Int. Ed.*, 2016, **128**, 6521–6526.
5 K. M. Fromm, *Coord. Chem. Rev.*, 2008, **252**, 856–885.
6 D. Banerjee, Z. Zhang, A. M. Plonka, J. Li and J. B. Parise, *Cryst. Growth Des.*, 2012, **12**, 2162–2165.
7 J. Cepeda, S. Pérez-YáÑez, G. Beobide, O. Castillo, E. Goikolea, F. Aguesse, L. Garrido, A. Luque and P. A. Wright, *Chem. Mater.*, 2016, **28**, 2519–2528.
8 A. S. Asha, M. Makkitaya, A. Sirohi, L. Yadav, G. Sheet and S. Mandal, *CrystEngComm*, 2016, **18**, 1046–1053.
9 A. Douvali, A. C. Tsipis, S. V. Eliseeva, S. Petoud, G. S. Papaefstathiou, C. D. Malliakas, I. Papadas, G. S. Armatas, I. Margiolaki, M. G. Kanatzidis, T. Lazarides and M. J. Manos, *Angew. Chem., Int. Ed.*, 2015, **127**, 1671–1676.
10 A. M. Plonka, X. Chen, H. Wang, R. Krishna, X. Dong, D. Banerjee, W. R. Woerner, Y. Han, J. Li and J. B. Parise, *Chem. Mater.*, 2016, **28**, 1636–1646.
11 A. Schneemann, V. Bon, I. Scwedler, I. Senkovska, S. Kaskel and R. A. Fischer, *Chem. Soc. Rev.*, 2014, **43**, 6062.
12 Z. J. Lin, J. Lü, M. Hong and R. Cao, *Chem. Soc. Rev.*, 2014, **43**, 5867–5895.
13 T. Liu, J. Lü, C. Tian, M. Cao, Z. Lin and R. Cao, *Inorg. Chem.*, 2011, **50**, 2264–2271.
14 S. Dang, E. Ma, Z. M. Sun and H. Zhang, *J. Mater. Chem.*, 2012, **22**, 16920.
15 Y. Lan, H. Jiang, S. Li and Q. Xu, *Adv. Mater.*, 2011, **23**, 5015–5020.
16 T. Tu, T. Maris and J. D. Wuest, *J. Org. Chem.*, 2008, **73**, 5255.
17 *Oxford Diffraction, CrysAlis CCD and CrysAlis RED*, OxfordDiffraction Ltd., Abingdon, UK, 2008.
18 M. C. Burla, R. Caliandro, M. Camalli, B. Carrozzini, G. L. Cascarano, L. De Caro, C. Giacovazzo, G. Polidori and R. Spagna, *J. Appl. Crystallogr.*, 2005, **38**, 381–388.
19 G. M. Sheldrick, *SHELXL-2014/7: Program for Refinement of Crystal Structures*, University of Göttingen, Germany, 2014.
20 L. J. Farrugia, *J. Appl. Crystallogr.*, 1999, **32**, 837–838.
21 A. L. Spek, *J. Appl. Crystallogr.*, 2003, **36**, 7–13.
22 *SADABS (Version 2016/2)*, Bruker AXS Inc., Madison, Wisconsin, USA.
23 K. M. Fromm, *Coord. Chem. Rev.*, 2008, **252**, 856–885.
24 Z. Guo, R. Cao, X. Wang, H. Li, W. Yuan, G. Wang, H. Wu and J. Li, *J. Am. Chem. Soc.*, 2009, **131**, 6894–6895.
25 J. Tian, R. K. Motkuri, P. K. Thallapally and B. P. McGrail, *Cryst. Growth Des.*, 2010, **10**, 5327–5333.
26 Z. Lin, J. Lu, M. Hong and R. Cao, *Chem. Soc. Rev.*, 2014, **43**, 5867–5895.
27 T. F. Liu, J. Lu, X. Lin and R. Cao, *Chem. Commun.*, 2010, **46**, 8439.
28 L. Du, Z. Lu, K. Zhang, J. Wang, X. Zheng, Y. Pan, X. You and J. Bai, *J. Am. Chem. Soc.*, 2012, **135**, 562–565.
29 B. Zheng, Z. Yang, J. Bai, Y. Li and S. Li, *Chem. Commun.*, 2012, **48**, 7025–7027.
30 B. Zheng, J. Bai, J. Duan, L. Wojtas and M. J. Zaworotko, *J. Am. Chem. Soc.*, 2010, **133**, 748–751.

31 Y. Lan, H. Jiang, S. Li and Q. Xu, *Adv. Mater.*, 2011, **23**, 5015–5020.
32 Q. Zhai, X. Bu, X. Zhao, C. Mao, F. Bu, X. Chen and P. Feng, *Cryst. Growth Des.*, 2016, **16**, 1261–1267.
33 X. Si, C. Jiao, F. Li, J. Zhang, S. Wang, S. Liu, Z. Li, L. Sun, F. Xu, Z. Gabelica and C. Schick, *Energy Environ. Sci.*, 2011, **4**, 4522–4527.
34 B. Zheng, Z. Yang, J. Bai, Y. Li and S. Li, *Chem. Commun.*, 2012, **48**, 7025–7027.
35 A. Yazaydin, A. I. Benin, S. A. Faheem, P. Jakubczak, J. J. Low, R. R. Willis and R. Q. Snurr, *Chem. Mater.*, 2009, **21**, 1425–1430.
36 Y. Lin, Q. Yan, C. Kong and L. Chen, *Sci. Rep.*, 2013, **3**, 1859.
37 J. Yu, L. Xie, J. Li, Y. Ma, J. M. Seminario and P. B. Balbuena, *Chem. Rev.*, 2017, **117**, 9674–9754.
38 S. Bourrelly, B. Moulin, A. Rivera, G. Maurin, S. Devautour-Vinot, C. Serre, T. Devic, P. Horcajada, A. Vimont, G. Clet, M. Daturi, J. Lavalley, S. Loera-Serna, R. Denoyel, P. L. Llewellyn and G. Férey, *J. Am. Chem. Soc.*, 2010, **132**, 9488–9498.
39 H. Furukawa, F. Gándra, Y. Zhang, J. Jiang, W. L. Queen, M. R. Hudson and O. M. Yaghi, *J. Am. Chem. Soc.*, 2014, **136**, 4369–4381.